Chinese Chemical Letters 34 (2023) 108228

Contents lists available at ScienceDirect

Chinese Chemical Letters

journal homepage: www.elsevier.com/locate/cclet

Halide/sulfide composite solid-state electrolyte for Li-anode based all-solid-state batteries

Haochang Zhang[a,b], Zhaozhe Yu[b,*], Jinyin Cheng[a,b], Hannan Chen[a], Xiao Huang[a,*], Bingbing Tian[a,*]

[a] International Collaborative Laboratory of 2D Materials for Optoelectronics Science and Technology of Ministry of Education, Institute of Microscale Optoelectronics, Shenzhen University, Shenzhen 518060, China
[b] Guangxi Key Laboratory of Manufacturing Systems and Advanced Manufacturing Technology, Guilin University of Electronic Technology, Guilin 541004, China

ARTICLE INFO

Article history:
Received 5 January 2023
Revised 30 January 2023
Accepted 14 February 2023
Available online 19 February 2023

Keywords:
Li_2ZrCl_6
Li_6PS_5Cl
Composite solid-state electrolyte
Interface stability
Li anode

ABSTRACT

Li_2ZrCl_6 (LZC) solid-state electrolytes (SSEs) have been recognized as a candidate halide SSEs for all-solid-state Li batteries (ASSLBs) with high energy density and safety due to its great compatibility with 4 V-class cathodes and low bill-of-material (BOM) cost. However, despite the benefits, the poor chemical/electrochemical stability of LZC against Li metal causes the deterioration of Li/LZC interface, which has a detrimental inhibition on Li^+ transport in ASSLBs. Herein, we report a composite SSE combining by LZC and argyrodite buffer layer (Li_6PS_5Cl, LPSC) that prevent the unfavorable interaction between LZC and Li metal. The Li/LPSC-LZC-LPSC/Li symmetric cell stably cycles for over 1000 h at 0.3 mA/cm^2 (0.15 mAh/cm^2) and has a high critical current density (CCD) value of 2.1 mA/cm^2 at 25 °C. Under high temperature (60 °C) which promotes the reaction between Li and LZC, symmetric cell fabricated with composite SSE also display stable cycling performance over 1200 h at 0.3 mAh/cm^2. Especially, the Li/NCM ASSLBs fabricated with composite SSE exhibit a high initial coulombic efficiency, as well as superior cycling and rate performance. This simple and efficient strategy will be instrumental in the development of halide-based high-performance ASSLBs.

Li-ion batteries (LIBs) have been infiltrated into our lives, due to their widespread applications in mobile phones, power supplies, electric vehicles and other fields [1–7]. However, the existing commercial LIBs employ liquid electrolytes, which leads to serious safety issues under harsh working conditions [8–11]. As one of the next-generation LIBs, the all-solid-state Li batteries (ASSLBs) have the potential to replace the liquid LIBs due to its extremely high safety and potentially high energy density [12–15]. Solid-state electrolytes (SSEs) are the key component in fabricating ASSLBs. A wide variety of SSEs including sulfides ($Li_{10}GeP_2S_{12}$ [16–21], Li-Argyrodites $Li_{7-x}PS_{6-x}Cl_x$ [22–27], $Li_7P_3S_{11}$ [28–30], β-Li_3PS_4 [31–33]), oxides (NASCION-type $Li_{1+x}Al_x(Ti/Ge)_{2-x}(PO_4)_3$ [19,34-36], garnet-type $Li_7La_3Zr_2O_{12}$ [37–42], perovskite-type $Li_{3+x}La_{2/3-x}TiO_3$ [43–45]), polymers (PEO [46–49], PVDF-HFP [50,51]) and halides (Li_3MX_6 [52–56], spinel-type $LiSc_{2/3}Cl_4$ [57,58], hexagonal close-packed (hcp) Li_2ZrCl_6 [59–62]) have been studied.

The halide SSEs have attracted more and more attention and been a hot-spot recently, owing to the good compatibility matching 4 V-class layered-structural cathodes and the softness in fabricating ASSLBs [1,60,63]. Especially, the hexagonal closest packed (hcp) Li_2ZrCl_6 (LZC) has become one of the halides SSEs with great commercialization potential and has attracted widespread attentions because of its extremely low material cost compared to other halide SSEs (Li_3InCl_6, Li_3ScCl_6, *etc.*). Meanwhile, the LZC still has the advantages of being relatively stable at elevated voltages (>4.3 V) due to the high oxidation potential of chloride anions [1]. For example, Ma *et al.* [59] and Jung *et al.* [60] synthesized the LZC by ball milling, and fabricated the ASSLBs with a direct contact between LZC and the 4 V-class cathode particles, which delivered initial coulombic efficiencies of 97.9% and 90.3% for $LiCoO_2$ (LCO) and single crystalized $LiNi_{0.8}Co_{0.1}Mn_{0.1}O_2$ (without any coating). Unlike the cathode interface, the [$ZrCl_6$] unit could be easily reduced, and therefore, LZC are generally unstable at the anode interface, especially in contact with Li metal anodes [64]. Recently, by examining the reaction products at the anode interface, Riegger

* Corresponding authors.
E-mail addresses: yuzhaozhe@guet.edu.cn (Z. Yu), xiao199198@gmail.com (X. Huang), tianbb2011@szu.edu.cn (B. Tian).

https://doi.org/10.1016/j.cclet.2023.108228
1001-8417/

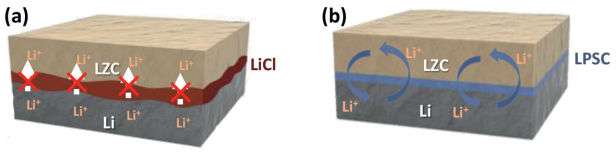

Scheme 1. Schematic illustration showing (a) pure LZC and (b) LPSC-LZC composite solid-state electrolyte in contact with Li anode.

[65] and Fu [66] succeeded in elucidating the mechanism of interaction between halides (Li_3MX_6) and Li metal. The high-valence metal cations (M^{3+} or M^{4+}) in halides can easily be reduced to M^0 by Li metal. However, this newly interface containing M^0 is still electronically conductive with low ionic conductivity, which hinders Li^+ transport and will continue expanding by continuously consuming Li metal and Li_3MX_6 [67].

Inspired by the crucial role that interfacial decomposition components played, we demonstrate a composite SSE composed of argyrodite buffer layer and LZC for the inhibition of reaction between Li and LZC. The Li_6PS_5Cl (LPSC) protective buffer layer has a high Li^+ conductivity (2–4 mS/cm) and low electronic conductivity (10^{-9}–10^{-8} S/cm) [3,24,68], which effectively suppresses the reduction and Li dendrites during electrochemical cycling. Importantly, the composite SSEs are expected to have excellent stability against Li metal (Scheme 1), where the interface and interphase were studied in details by X-ray diffraction (XRD), X-ray photoelectron spectroscopy (XPS), scanning electron microscopy (SEM), and Raman spectroscopy measurements. What is more, the Li/Li symmetric cells were tested at different currents and temperatures to further demonstrate the stability of this composite SSE. Finally, the composite SSE based ASSLBs that employ Li metal as anode were fabricated and examined to verify the successful application of composite SSE. Our work provides simple and effective method solving the side reactions between Li anode and LZC halide SSE, which promotes the development of all-solid-state batteries.

To prepare Li_2ZrCl_6 (LZC), a stoichiometric mixture (10 g) of LiCl (anhydrous, 99%, Aladdin), $ZrCl_4$ (anhydrous, 99.9%, Aladdin), was ball-milled at 250 rpm for 32 h in a ZrO_2 tank (500 mL, inner dimensions: φ 89 × h 88 mm) with ZrO_2 balls (φ 10 mm, 250 g, CNPOWDER, Zhuzhou) using MITR-YXQM-8L. Li_6PS_5Cl (LPSC) was synthesized by a procedure of ball-milling and subsequent annealing. The stoichiometric mixture (15 g) of LiCl (anhydrous, 99%, Aladdin), Li_2S (anhydrous, 99.9%, HangZhou KaiYaDa Semiconductor Materials Co., Ltd.) and P_2S_5 (anhydrous, 99%, Macklin) were ball-milled at 180 rpm for 6 h in a Polyurethane tank (500 mL, inner dimensions: φ 89 × h 88 mm) with ZrO_2 balls (φ 10 mm, 150 g) using MITR-YXQM-8L. After ball-milling process, the mixture was sealed in a quartz bottle and annealed at 460 °C (heating rate of 1 °C/min) for 14 h and then natural cooled to obtain the final Li_6PS_5Cl. All above operations were carried out under argon atmosphere. The composite SSEs were prepared by cold press. Firstly, cold press the LZC powder (100 mg) under 240 MPa pressure, and then LPSC powder (15 mg) was spread on one side of LZC pellet and cold pressed under 300 MPa.

XRD cells holding hermetically sealed SSE powders with a PI film were carried on an XRD diffractometer (Ultima IV) and measured at 40 kV and 40 mA from 10° to 60° with a scan speed of 2.4°/min. The PHI 5000 Versa Probe III used a monochromatic Al K X-ray source with a 200 μm beam size to conduct X-ray photoelectron spectroscopy (XPS). Dual beam charge neutralization was used to achieve charge compensation, and the hydrocarbon C 1s feature's binding energy was adjusted to 284.8 eV to rectify the binding energy. Energy dispersive spectroscopy (EDS, Bruker) was added to scanning electron microscopy (SEM, TESCAN MIRA3) in order to analyze the morphologies or elemental distributions, respectively. Raman spectra were collected with an Ar-ion laser beam at exciting radiation wavelength of 514 nm using a laser Raman spectrometer (AW200SG, Electrotek).

All-solid-state Li batteries fabrications: the synthesized powder was loaded into an electrically insulating Al_2O_3 cylindrical cell with an inner diameter of φ 10 mm, and then was compressed under 240 MPa without heat treatment. Carbon electrodes were then added on both sides, and the C/SSEs/C symmetric cell was used for the AC impedance test. An electrochemical workstation (IVIUM nSTAT) was used to measure the electrochemical impedance spectroscopy (EIS) with a frequency range of 1 MHz to 1 Hz and an amplitude of 10 mV. The conventional formula, $\sigma = L/RS$, where L is the pellet's thickness, S is its area, and R is the resistance value determined by the EIS test, yields the conductivity value σ. The EIS test at varied temperatures from −15 °C to 65 °C was conducted using the In/SSEs/In symmetric cell *via* Zahner Zennium pro with a frequency range of 5 MHz-1 Hz, where measurements were conducted continuously from low to high temperatures being monitored by the HHTC-30–40-F. Li metal was employed as the anode for the ASSLBs. LCO or $LiNi_{0.6}Co_{0.2}Mn_{0.2}O_2$ (NCM622), SSEs, and super C65 (annealed at 800 °C for 12 h) powders were mixed at a weight ratio of 70:30:2 to prepare composite working electrodes. In the battery assembly procedure, we first pressed SSEs at 240 MPa, then added a thin LPSC layer on one side of the electrolyte and pressed the composite cathode at 300 MPa. Finally, Li anode was added on the LPSC side, and the entire assembled ASSLBs was kept at approximately 30 MPa in test moulds. The full cells were evaluated by a Neware battery testing equipment (CT-4008–5V10mA-164) in voltage ranges of 3.0–4.3 V for LCO/NCM622.

The LZC was synthesized through LiCl and $ZrCl_4$ by high energy ball milling. The XRD patterns of LZC showed a high matching with Li_3YCl_6 (PDF#44–0286), except for a position shift of the peak caused by the different ionic radii of Zr^{4+} and Y^{3+} (Fig. 1a). Meanwhile, the Arrhenius plot of the LZC in the temperature range from −15 °C to 65 °C are shown in Fig. 1b, delivering good linearity and the corresponding activation energy (E_a) was 0.424 eV. Nyquist plots at all temperatures and corresponding distribution of relaxation time (DRT) are shown in Figs. S2 and S3 (Supporting information). Nyquist plots of LZC and LPSC at −15∼65 °C were fitted to the model $Z_{DRT}(f) = R_\infty + \int_0^\infty \gamma ln\tau/(1 + i\pi f\tau)dln\tau$, where R_∞ denotes the ohmic resistance, τ is the relaxation time, and $\gamma ln\tau$ is the distribution function of relaxation times (written as $\gamma(\tau)$). As the temperature increased, the resistance and DRT's relaxation time of LZC decreased. The EIS spectra of LZC at 25 °C is shown inset of Fig. 1b, where the Li^+ conductivity was 0.33 mS/cm and the electronic conductivity was 2.48×10^{-9} S/cm (Fig. S4 in Supporting information). What is more, the SEM images of LZC powder are depicted in Fig. S5 (Supporting information). Although the grain sizes of LZC powder were non-uniform, all powders no matter in agglomerations or single particles were less than 500 nm. Meanwhile, Fig. S6 (Supporting information) shows the energy dispersive X-ray spectroscopy (EDS) mapping for cross-sectional of LZC pellet, illustrating the uniform distribution of Zr, Cl elements in LZC. The above results demonstrate that the LZC halide SSEs were successfully synthesized. Owing to the high Li^+ conductivity, low electronic conductivity and the ability to form a stable interfacial layer in contact with Li metal, the LPSC was selected as the buffer layer with LZC to form composite SSEs to prevent the unfavorable reaction between LZC and Li metal. LPSC was synthesized through conventional milling-calcination solid reaction method. Fig. 1c displays the pure argyrodite-phase of LPSC, and its Li^+ conductivity, electronic conductivity and E_a were 2.4 mS/cm (inset of Fig. 1d), 2.89×10^{-9} S/cm (Fig. S7 in Supporting information), and 0.385 eV (Fig. 1d), respectively. Corresponding Nyquist plots and DRT results were shown in Figs. S8 and S9 (Supporting information). As de-

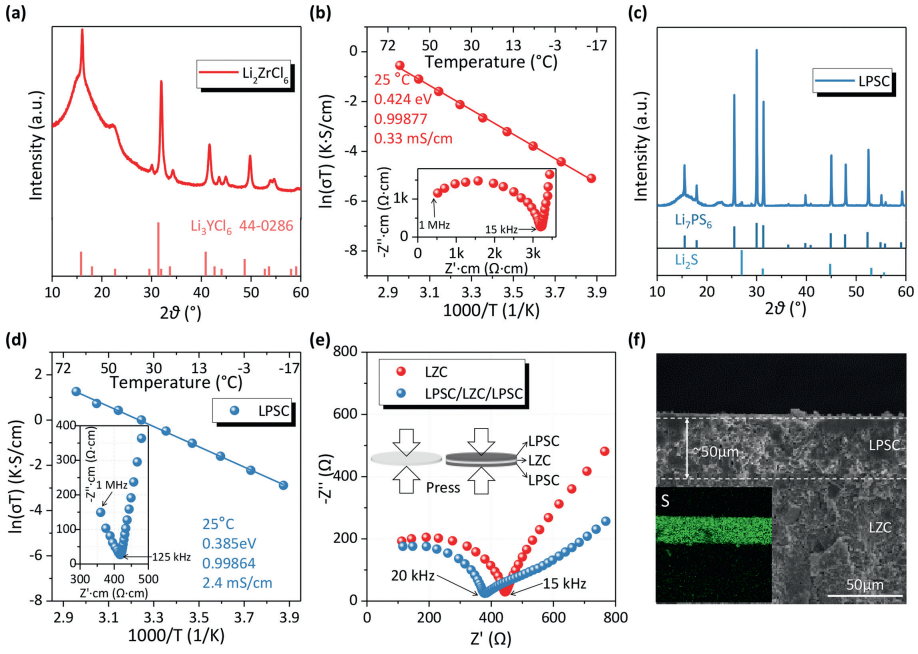

Fig. 1. (a) XRD pattern of LZC. Bragg indexes for Li_3YCl_6 (44-0286) is shown at the bottom. (b) Arrhenius plot and Nyquist plot of LZC at 25 °C in the inset. (c) XRD pattern of LPSC. Bragg indexes for Li_7PS_6 and Li_2S are shown at the bottom. (d) Arrhenius plot and Nyquist plot of LPSC at 25 °C in the inset. (e) EIS plots of LZC and LPSC-LZC-LPSC at 25 °C. (f) Cross-section SEM image of the LPSC-LZC and the corresponding EDS mapping of S element.

picted in Figs. S10 and S11 (Supporting information), the particle sizes of LPSC powders were in agglomeration in several microns with the primary particles and the P, S and Cl elements were uniformly distributed in the LPSC.

The composite SSE was synthesized by cold pressing at 240 MPa. The SEM images of composite SSE and corresponding EDS mappings of S are shown in Fig. 1f. The thickness of LPSC layer was approximately 50 μm. To verify the compatibility between LZC and LPSC, the Li^+ conductivities of LZC and LPSC-LZC-LPSC were tested (Fig. 1e), where no much difference was observed, indicating that the interfacial resistance of LZC/LPSC was low. Interestingly, the resistance of the composite electrolyte is smaller than that of LZC itself. Owing to the better mechanical flexibility of LPSC than that of LZC, LPSC is in closer contact with the blocking electrode (carbon, C) than that of LZC. Moreover, the contact resistance between C and LPSC is also smaller than that of C and LZC due to the better mechanical flexibility of LPSC. So the as tested resistance of the composite electrolyte is smaller than that of LZC itself. Meanwhile, errors in the testing process and of test equipment may also contribute to this result. Meanwhile, we mixed the LZC and LPSC powders and stored for 24 h. XRD patterns of the mixed powders do not change before and after mixing (Fig. S12 in Supporting information), indicating that the LZC and LPSC co-exist without any side reaction. All results indicated that the composite SSE is stable.

The symmetric Li/Li cells were assembled to further investigate the chemical and electrochemical stability between the composite SSE and Li metal. Figs. 2a and b show the impedance evolution during the storage (without charging/discharging) of Li/LZC/Li and Li/LPSC-LZC-LPSC/Li cells. The resistance of Li/LZC/Li cell increased gradually with time (732 Ω to 6329 Ω in 96 h), indicating the Li/LZC interface was worsening during storage. In stark contrast, the composite SSE demonstrated good compatibility with Li metal, where the resistance of Li/LPSC-LZC-LPSC/Li symmetric cell hardly altered in 96 h (Fig. 2b). Additionally, DRT tool [69,70] was applied to further analyze the Nyquist plots of symmetric cells. As shown in Fig. 2c, the τ at 10^{-6} s represented the Li^+ migration in SSE [69], where the τ and resistance of Li/LZC/Li and Li/LPSC-LZC-LPSC/Li were similar. However, the τ of Li/LZC/Li became sluggish and the impendence increased very large after 96 h of aging, while Li/LPSC-LZC-LPSC/Li almost unchanged. Obviously, the LPSC layer worked very well for preventing the unfavorable reaction between LZC and Li metal. To further evaluate the electrochemical stability of composite SSE against Li metal, the stripping/plating measurements were carried out in symmetric Li/Li cells, as shown in Fig. 2d. At room temperature (25 °C), the Li/LZC/Li symmetric cell delivered a rapid increase in overpotential to 1 V at 0.3 mA/cm^2 (0.15 mAh/cm^2) within 60 h, suggesting that reaction products had accumulated to impede the charge transfer at the Li/LZC interface. In contrast, the Li/LPSC-LZC-LPSC/Li symmetric cell delivered excellent stability during cycling over 1000 h (Fig. 2d), where the polarization voltage slightly increased from 90 mV to 119 mV (inset of Fig. 2d), indicating the good stability of interface toward Li metal and highly stable reversibility of Li anode. Meanwhile, the composite SSE still had stability against Li at high temperature (60 °C), where the Li/Li symmetric cell for composite SSE exhibited a stable cycling and low polarization voltage for 1200 h at 0.3 mAh/cm^2 (Fig. 2e) and 500 h at 0.5 mAh/cm^2 (Fig. S13 in Supporting information). Furthermore, the rate performance of Li/Li symmetric cells of LZC and composite SSE was tested from 0.05 mA to 1.7 mA (Figs. 2f and g). When the current increased to 0.85 mA (1.08 mA/cm^2), the polarization voltage of Li/LZC/Li increased to the protection voltage 4 V. However, when the polarization voltage of Li/LPSC-LZC-LPSC/Li increased to 4 V, the CCD was as high as 2.1 mA/cm^2 (1.65 mA), which further proves the great electrochemical stability of composite SSE against Li metal.

Cross-sectional SEM images of Li/LZC/Li and Li/LPSC-LZC-LPSC/Li symmetric cells after 50 h of cycling are shown in Figs. 3a and b. The Li/LZC interface underwent serious side reactions, where cracks due to the volume expansion of Li metal were clearly observed. By introducing LPSC combined with LZC to form composite SSE, the symmetric cell maintained a continuous and robust interface. Corresponding EDS mapping of S and Cl elements further revealed uniform distribution, indicating the robust interface between composite SSE and Li anode (Fig. 3c). In addition, digital

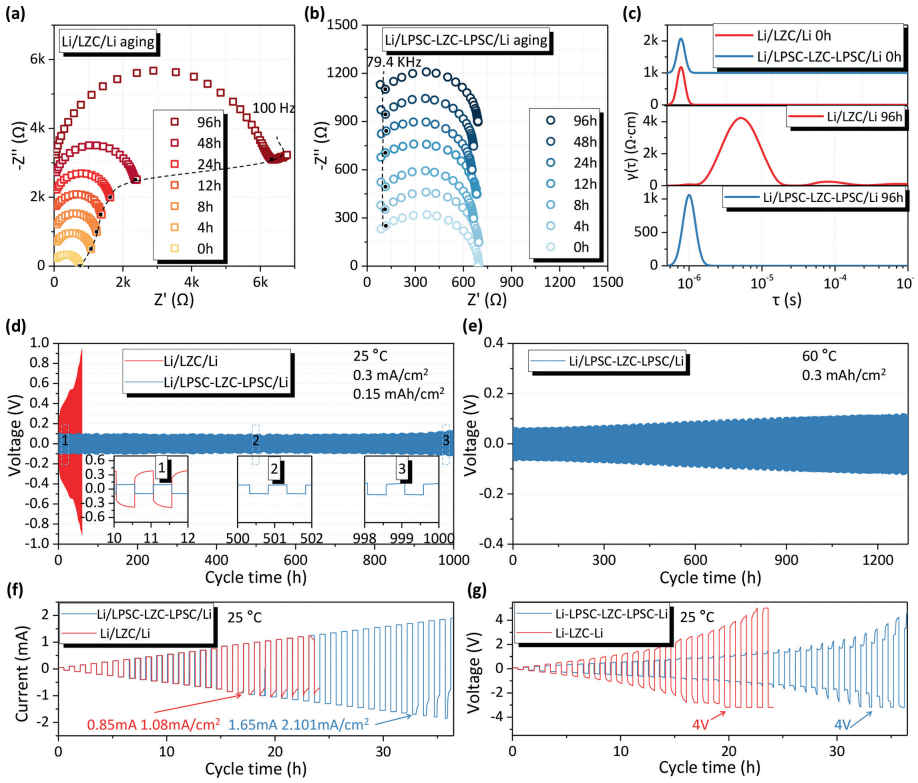

Fig. 2. EIS spectra of (a) Li/LZC/Li and (b) Li/LSPC-LZC-LPSC/Li after aging. (c) DRT results corresponding to Nyquist plots in (a, b). (d) Li plating/stripping voltage curves of the symmetric cells at 0.3 mA/cm^2 (0.15 mAh/cm^2) and 25 °C. The details are indicated by the 1, 2 and 3 areas marked in the inset. (e) Li plating/stripping voltage curves of the Li/LPSC-LZC-LPSC/Li cell at 0.3 mAh/cm^2 and 60 °C. (f) Current and (g) voltage profile of the symmetric cells at increasing stepwise current densities and the duration for each charge and discharge step was 0.5 h.

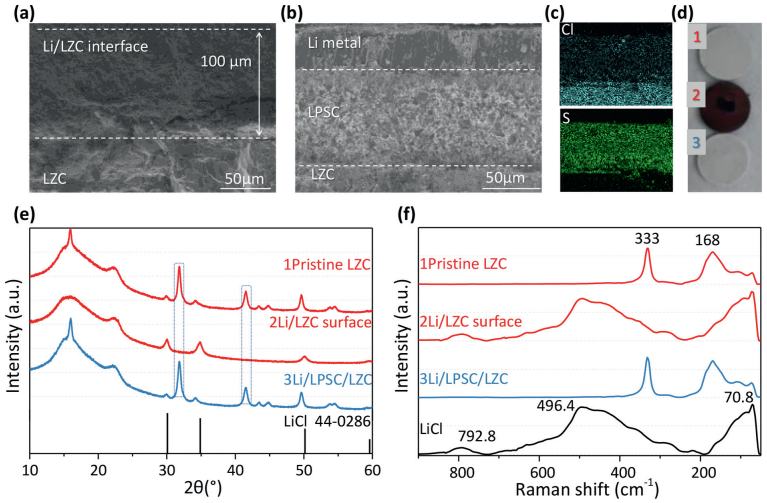

Fig. 3. Cross-sectional SEM images of (a) Li/LZC/Li and (b) Li/LPSC-LZC-LPSC/Li after 50 h cycling. (c) EDS mapping of Cl and S at the cross-section as shown in (b). (d) The digital images (1–3) of (1) pristine LZC, (2) LZC reacted with Li, and (3) LZC protected with LPSC, respectively, after cycling. (e) Surficial XRD patterns and (f) Raman spectra of (1–3) as denoted above.

images clearly demonstrated that the surface of pure LZC turned black after cycling with Li metal, whereas the LZC protected by LPSC was essentially unaltered, demonstrating the excellent compatibility of composite SSE against Li (Fig. 3d). After direct contact of LZC and Li, the LZC phase of blackened materials matched exactly with the LiCl, indicating that LZC had been completely reduced by Li metal. The XRD patterns of LZC with LPSC after reaction with Li metal was almost the same to the pristine LZC, indicating no side reaction (Fig. 3e). The results of Raman (Fig. 3f) were similar to that of XRD, the characteristic wave numbers of blackened LZC (2) were 792.8, 496.4 and 70.8 cm^{-1}, which matched with LiCl. The Raman shift of LZC with LPSC protection (3) was identical to that of pure LZC (1).

To further investigate the reaction mechanism of LZC with Li metal and the protective effect of LPSC on LZC, XPS were performed to analyze the Li/LZC interface and Li/LPSC-LZC interface after cycling (Fig. 4). LZC was reduced by Li metal to Zr and LiCl, which explained the increasing overpotential during the platting/stripping process. As a sharp comparison, the XPS spectra of LZC protected by LPSC had barely changed, remaining the same as

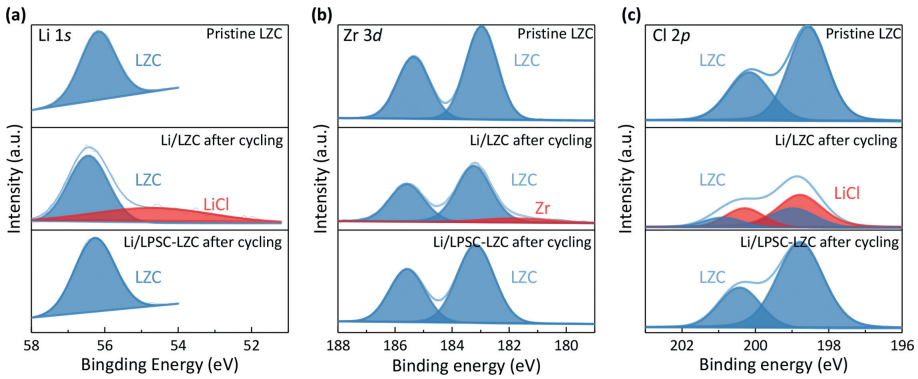

Fig. 4. XPS spectra of pristine LZC, Li/LZC and Li/LPSC-LZC after 50 h cycling. (a) Li 1s, (b) Zr 3d and (c) Cl 2p.

the pristine LZC (Fig. 4). Besides, the LPSC powder and Li pieces were hand-mixing for 20 min at a molar ratio 1:8 to explore the reaction mechanism of the Li/LPSC interface. The XRD pattern of Li/LPSC was largely identical to that of pristine LPSC (Fig. S14 in Supporting information). Meanwhile, the Li/LPSC interface and pure LPSC were also investigate by XPS. Compared with LPSC, Li/LPSC interface only delivered partial Li_2S as well as phosphorus sulfide with no serious reduction reactions, indicating that a stable interface formed when LPSC contacting to Li metal (Fig. S15 in Supporting information).

To assess the benefit of composite SSE in a ASSLBs, Li/LPSC-LZC/$LiCoO_2$ (LCO) and Li/LPSC-LZC/$LiNi_{0.6}Co_{0.2}Mn_{0.2}O_2$ (NCM622) full cells were assembled and evaluated. The Li/LPSC-LZC/LCO cell delivered much higher initial coulombic efficiency (96.1%) than that of the Li/LZC/LCO cell (89.9%) (Fig. 5a). In addition, initial charge/discharge curve of the Li/LZC/LCO cell delivered a much lower voltage than that of Li/LPSC-LZC/LCO. The Li/LZC/LCO cell also delivered a rapid capacity fading from 152.9 mAh/g to 45 mAh/g within 3 cycles at an LCO loading of 6 mg/cm^2 and 0.1 C rate (Fig. 5b), which was caused by the serious side reaction between LZC and Li metal. In comparison, the Li/LPSC-LZC/LCO cell displayed good cycling stability over 70 cycles with 80.5% capacity retention and a high coulombic efficiency of ~100%. Fig. S16a (Supporting information) displays the rate capacity of Li/LPSC-LZC/LCO and the corresponding charge/discharge curves are shown in Fig. S16b (Supporting information). In addition, the Li/LPSC-LZC/NCM622 cell delivered good rate performance, where the specific capacities at 0.1, 0.3, 0.5 and 1 C were 187.5, 162.5, 133.2 and 66.4 mAh/g, respectively (Fig. 5c). The corresponding charge/discharge curves are shown in Fig. S17 (Supporting information). Moreover, the cycling performance of Li/LPSC-LZC/NCM622 cell is shown in Fig. 5d. The cell presented a specific capacity of 158.8 mAh/g at 0.3 C with a capacity retention ratio of 87.1% after 70 cycles. However, the Li/LZC/NCM622 cell cannot work owing to the seriously deteriorated Li/LZC interface (Fig. S18 in Supporting information). All of these findings prove the superior stability and reversibility of the ASSLBs fabricated with composite SSE and Li anode.

In summary, we propose a composite SSE combining the LZC and argyrodite buffer layer (LPSC). The LPSC's high Li^+ conductivity (2.4 mS/cm) and low electronic conductivity (2.89×10^{-9} S/cm) enable it to act as a bridge between LZC and Li. SEM, XRD and Raman spectroscopy results clearly demonstrated the stability of composite SSE against Li metal. Therefore, the Li/LPSC-LZC-LPSC/Li symmetrical cell exhibited stable cycling over 1000 h at 0.3 mA/cm^2 (0.15 mAh/cm^2) and a high CCD value of 2.1 mA/cm^2 at 25 °C. Meanwhile, the composite SSE based ASSLBs which employ Li metal as an anode display high coulombic efficiency (~100%), outstanding cycling (>70 cycles) and rate performance (>120 mAh/g at 0.5 C). This work provides a simple and practical method for the application of halide-based SSE in Li-anode based ASSLBs.

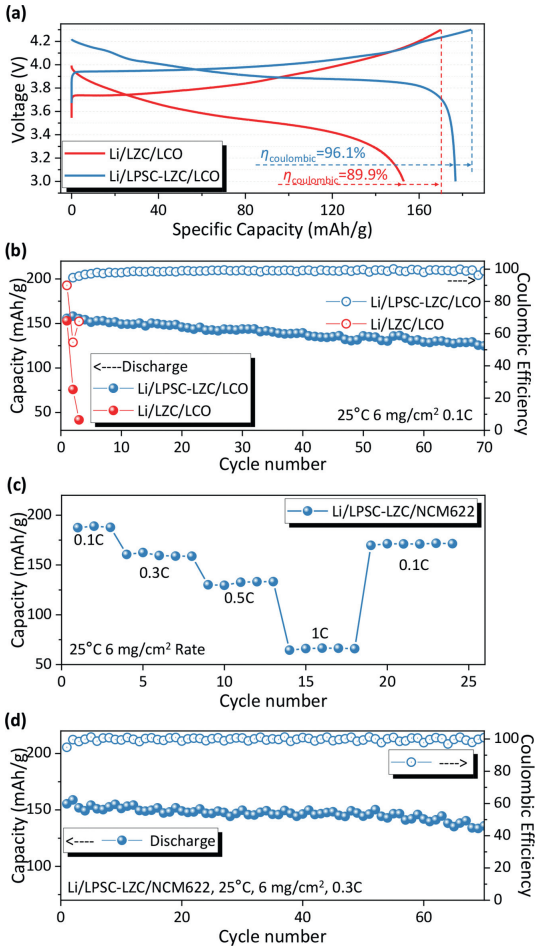

Fig. 5. Electrochemical performance of the ASSLBs employing LZC and composite SSE at 25 °C. (a) Initial charge/discharge curves obtained at 0.1 C for LCO electrodes using LZC and composite SSE with the coulombic efficiency denoted as $\eta_{coulomb}$, and (b) corresponding long-term cycling performance at 0.1 C. (c) Rate performance of NCM622 electrodes using composite SSE at 0.1, 0.3, 0.5 and 1 C, and (d) long-term cycling performance thereof at 0.3 C.

Declaration of competing interest

The authors declare that they have no known competing financial interests or personal relationships that could have appeared to influence the work reported in this paper.

Acknowledgments

B. Tian acknowledges the financial support from the Science and Technology Project of Shenzhen (No. JCYJ20210324094206019). X. Huang acknowledges the financial support from the National Natural Science Foundation of China (No. 52102284). Z. Yu acknowledges Department of Science and Technology of Guangxi Province (Nos. AB21220027, AD19110077), Guangxi Key Laboratory of Manufacturing Systems Foundation (No. 20-065-40-005Z), Engineering Research Center Foundation of Electronic Information Materials and Devices (No. EIMD-AA202005).

Supplementary materials

Supplementary material associated with this article can be found, in the online version, at doi:10.1016/j.cclet.2023.108228.

References

[1] J.L.C. Wang, J.T. Kim, X.L. Sun, Sci. Adv. 8 (2022) eadc9516.
[2] Y. Lu, C.Z. Zhao, H. Yuan, et al., Matter 5 (2022) 876–898.
[3] C. Yu, F.P. Zhao, J. Luo, L. Zhang, X.L. Sun, Nano Energy 83 (2021) 105858.
[4] S.A. Peryez, M.A. Cambaz, V. Thangadurai, M. Fichtnert, ACS Appl. Mater. Interfaces 11 (2019) 22029–22050.
[5] Y. Kong, X. Ao, X. Huang, et al., Adv. Sci. 9 (2022) e2105538.
[6] S. Yang, B. Wang, Q. Lv, et al., Chin. Chem. Lett. 34 (2023) 107783.
[7] C. Li, R. Liu, S. Zhang, et al., Chin. Chem. Lett. 34 (2023) 108083.
[8] Y. Meesala, A. Jena, H. Chang, R.S. Liu, ACS Energy Lett. 2 (2017) 2734–2751.
[9] Q. Kang, Y. Li, Z. Zhuang, et al., J. Energy Chem. 69 (2022) 194–204.
[10] Y. Lu, C.Z. Zhao, H. Yuan, et al., Adv. Funct. Mater. (2021) 2009925.
[11] Y. Xiao, Y. Wang, S.H. Bo, et al., Nat. Rev. Mater. 5 (2019) 105–126.
[12] Y. Niu, Z. Yu, Y. Zhou, et al., Nano Res. 15 (2022) 7180–7189.
[13] X. Huang, Y. Lu, Z. Song, et al., Energy Storage Mater. 22 (2019) 207–217.
[14] L. Katzenmeier, S. Helmer, S. Braxmeier, E. Knobbe, A.S. Bandarenka, ACS Appl. Mater. Interfaces 13 (2021) 5853–5860.
[15] S.J. Chen, D.J. Xie, G.Z. Liu, et al., Energy Storage Mater. 14 (2018) 58–74.
[16] M.A. Philip, P.T. Sullivan, R. Zhang, et al., ACS Appl. Mater. Interfaces 11 (2019) 2014–2021.
[17] W. Zhang, T. Leichtweiss, S.P. Culver, et al., ACS Appl. Mater. Interfaces 9 (2017) 35888–35896.
[18] W. Cho, J. Park, K. Kim, J.S. Yu, G. Jeong, Small 17 (2021) e1902138.
[19] Y.L. Liu, Q. Sun, J.R. Liu, et al., ACS Appl. Mater. Interfaces 12 (2020) 2293–2298.
[20] H.L. Wan, S.F. Liu, T. Deng, et al., ACS Energy Lett. 6 (2021) 862–868.
[21] G. Liu, W. Weng, Z. Zhang, et al., Nano Lett. 20 (2020) 6660–6665.
[22] W. Ji, D. Zheng, X. Zhang, T. Ding, D. Qu, J. Mater. Chem. A 9 (2021) 15012–15018.
[23] L. Peng, H. Ren, J. Zhang, et al., Energy Storage Mater. 43 (2021) 53–61.
[24] S.H. Jung, U.H. Kim, J.H. Kim, et al., Adv. Energy Mater. (2019) 1903360.
[25] A.L. Hwang, Y.L. Ma, Y. Cao, et al., Int. J. Electrochem. Sci. 12 (2017) 7795–7806.
[26] T. Cheng, B.V. Merinov, S. Morozov, W.A. Goddard, ACS Energy Lett. 2 (2017) 1454–1459.
[27] J. Wu, L. Shen, Z. Zhang, et al., Electrochem. Energy Rev. 4 (2020) 101–135.
[28] G. Homann, P. Meister, L. Stolz, et al., ACS Appl. Energy Mater. 3 (2020) 3162–3168.
[29] C. Yu, L. van Eijck, S. Ganapathy, M. Wagemaker, Electrochim. Acta 215 (2016) 93–99.
[30] C. Yu, S. Ganapathy, E.R.H. Van Eck, et al., Nat. Commun. 8 (2017) 1086–1095.
[31] F. Marchini, S. Saha, D.A.D. Corte, J.M. Tarascon, ACS Appl. Mater. Interfaces 12 (2020) 15145–15154.
[32] Y. Yang, Q. Wu, Y. Cui, et al., ACS Appl. Mater. Interfaces 8 (2016) 25229–25242.
[33] J.G. Smith, D.J. Siegel, Nat. Commun. 11 (2020) 1483.
[34] T. Yoshinari, R. Koerver, P. Hofmann, et al., ACS Appl. Mater. Interfaces 11 (2019) 23244–23253.
[35] Y. Liu, C. Li, B. Li, et al., Adv. Energy Mater. 8 (2018) 1702374.
[36] X.F. He, Y.Z. Zhu, Y.F. Mo, Nat. Commun. 8 (2017) 15893–15900.
[37] X. Huang, Z. Song, T. Xiu, M.E. Badding, Z. Wen, Ceram. Int. 45 (2019) 56–63.
[38] L. Yang, Q.S. Dai, L. Liu, et al., Ceram. Int. 46 (2020) 10917–10924.
[39] X. Huang, J. Su, Z. Song, et al., Ceram. Int. 47 (2021) 2123–2130.
[40] M. Kotobuki, M. Koishi, Ceram. Int. 40 (2014) 5043–5047.
[41] X. Huang, C. Shen, K. Rui, et al., JOM 68 (2016) 2593–2600.
[42] Y. Zhou, X. Li, Y. Yang, X. Huang, B. Tian, ACS Appl. Energy Mater. 5 (2022) 13817–13828.
[43] L. Zhang, X.H. Zhang, G.Y. Tian, et al., Nat. Commun. 11 (2020) 3490–3498.
[44] A.La Monaca, A. Paolella, A. Guerfi, F. Rosei, K. Zaghib, Electrochem. Commun. 104 (2019) 106483.
[45] Z.Y. Jiang, H.Q. Xie, S.Q. Wang, et al., Adv. Energy Mater. 8 (2018) 1801433.
[46] Y. An, X. Han, Y. Liu, et al., Small 18 (2022) e2103617.
[47] J. Tan, X. Ao, H. Zhuo, et al., Chem. Eng. J. 420 (2021) 127623–127630.
[48] X. Ao, X. Wang, J. Tan, et al., Nano Energy 79 (2021) 105475–105485.
[49] M. Ge, X. Zhou, Y. Qin, et al., Chin. Chem. Lett. 33 (2022) 3894–3898.
[50] W.Q. Zhang, J.H. Nie, F. Li, Z.L. Wang, C.Q. Sun, Nano Energy 45 (2018) 413–419.
[51] J. Lu, Y.C. Liu, P.H. Yao, et al., Chem. Eng. J. 367 (2019) 230–238.
[52] G. Xu, L. Luo, J. Liang, et al., Nano Energy 92 (2021) 106674.
[53] X. Li, J. Liang, J. Luo, et al., Energy Environ. Sci. 12 (2019) 2665–2671.
[54] X. Li, J. Liang, N. Chen, et al., Angew. Chem. Int. Ed. 58 (2019) 16427–16432.
[55] S. Wang, X. Xu, C. Cui, et al., Adv. Funct. Mater. 32 (2021) 2108805.
[56] T. Asano, A. Sakai, S. Ouchi, et al., Adv. Mater. 30 (2018) e1803075.
[57] L. Zhou, T.T. Zuo, C.Y. Kwok, et al., Nat. Energy 7 (2022) 83–93.
[58] L. Zhou, C.Y. Kwok, A. Shyamsunder, et al., Energy Environ. Sci. 13 (2020) 2056–2063.
[59] K. Wang, Q. Ren, Z. Gu, et al., Nat. Commun. 12 (2021) 4410–4421.
[60] H. Kwak, D. Han, J. Lyoo, et al., Adv. Energy Mater. 11 (2021) 2003190.
[61] X. Luo, Y. Zhong, X. Wang, X. Xia, C. Gu, J. Tu, ACS Appl. Mater Interfaces 14 (2022) 49839–49846.
[62] H. Zhang, Z. Yu, H. Chen, et al., J. Energy Chem. 79 (2023) 348–356.
[63] Y. Wang, J. Liang, X. Song, Z. Jin, Energy Storage Mater. 54 (2023) 732–775.
[64] Y. Zhang, C. Sun, ACS Appl. Mater. Interfaces 13 (2021) 12099–12105.
[65] L.M. Riegger, R. Schlem, J. Sann, W.G. Zeier, J. Janek, Angew. Chem. Int. Ed. 60 (2021) 6718–6723.
[66] Y. Fu, C. Ma, Sci. China Mater. 64 (2021) 1378–1385.
[67] F. Han, Y. Zhu, X. He, Y. Mo, C. Wang, Adv. Energy Mater. 6 (2016) 139–159.
[68] J. Wu, S. Liu, F. Han, X. Yao, C. Wang, Adv. Mater. 33 (2021) e2000751.
[69] Y. Lu, C.Z. Zhao, J.Q. Huang, Q. Zhang, Joule 6 (2022) 1172–1198.
[70] M. Hahn, D. Rosenbach, A. Krimalowski, et al., Electrochim. Acta 344 (2020) 17.